Spatial positioning effect of dual cocatalysts accelerating charge transfer in three dimensionally ordered macroporous g-C$_3$N$_4$ for photocatalytic hydrogen evolution

Bo Lin, Jiali Li, Baorong Xu, Xiaoqing Yan, Bolun Yang, Jinjia Wei, Guidong Yang[*]

XJTU-Oxford Joint International Research Laboratory of Catalysis, School of Chemical Engineering and Technology, Xi'an Jiaotong University, Xi'an, Shaanxi 710049, China

ABSTRACT

The relatively low charge transfer efficiency remains the critical limiting factor for the practical application of solar-driven water splitting. In this work, a promising photocatalyst intensified by dual cocatalysts was developed via separately loading Au nanoparticles and CoP nanosheets onto the inside and outside surface of three dimensionally ordered macroporous (3DOM) g-C$_3$N$_4$ framework to significantly facilitate the ordered transfer of charges. The spatial positioning of dual cocatalysts and average wall thickness of 3DOM g-C$_3$N$_4$ framework were precisely controlled to reveal the optimal distribution position of Au and CoP as well as the most appropriate transfer distance for charges (from 3DOM g-C$_3$N$_4$ walls to the surface of cocatalysts), respectively. The results show that the spatial positioning effect of dual cocatalysts and optimization of charge transfer distance can endow the CoP/3DOM g-C$_3$N$_4$/Au photocatalyst with an excellent charge transfer efficiency, thereby contributing to high apparent quantum efficiency (AQE, 27.6% at 435 nm and 29.9% at 550 nm) and photocatalytic H$_2$ evolution activity of 11,820.1 μmol h^{-1} g^{-1}, which is up to 619.9, 6.5 and 5.6 times than that of 3DOM g-C$_3$N$_4$, CoP/3DOM g-C$_3$N$_4$ and 3DOM g-C$_3$N$_4$/Au, respectively. This work would provide a new platform to design high-performance artificial photocatalysts with superior charge transfer capacity.

1. Introduction

Solar-driven water splitting for hydrogen generation has been considered as an ideal and green pathway to deal with the global energy crisis [1–3], yet the relatively low charge transfer efficiency of routine semiconductor photocatalysts remains the critical limiting factor for its practical implementation [4–6]. From this perspective, loading cocatalyst on the surface of semiconductor photocatalysts, especially loading of dual cocatalysts, is known to have huge advantages for maximizing the extraction of charges and accelerate their transfer due to the presence of massive charge trapping sites on the surface of co-catalysts, thereby achieving the desirable activity of photocatalytic H$_2$ evolution over main photocatalysts [7–9]. Unfortunately, the general loading routes of dual cocatalysts are extremely easy to produce the random spatial positioning of cocatalysts on the surface of main photocatalysts, thus resulting in an inefficient migration of charges, eventually decreasing the photocatalytic activity [10–12]. More recently, it is reported that constructing dual cocatalysts with spatially separated positioning on the main photocatalyst surface is an effective approach

to address the above bottleneck, and several spherical nanostructured photocatalysts with spatially separated dual cocatalysts have been successfully constructed due to their feasible preparation process [13–15]. However, grafting dual cocatalysts with spatially separated positioning onto the other special microstructures remains a severe challenge, such as three dimensionally ordered macroporous (3DOM) microstructure, which is emerging as a promising opened-up architecture in photocatalysis due to its strong visible-light harvesting ability, efficient charge transfer as well as large active surface area [16–20].

In 2016, our group first reported the construction of well-defined 3DOM g-C$_3$N$_4$ by a simple thermal condensation-assisted colloidal crystal template method [16]. Although the charge transfer efficiency as well as the photocatalytic activity of single-component 3DOM g-C$_3$N$_4$ were significantly improved in comparison with g-C$_3$N$_4$ nanoparticles, its performances are still less than satisfactory, due to the random electron movement on the inside of 3DOM g-C$_3$N$_4$ framework [16]. However, the 3DOM architecture of g-C$_3$N$_4$ can be acted as an ideal host scaffold for constructing the dual cocatalysts with spatially

separated positioning to further promote the ordered charge transfer and enhance its photocatalytic activity in H_2 evolution. Therefore, in this article, the novel CoP/3DOM g-C_3N_4/Au photocatalyst (ACC) was constructed through loading Au nanoparticles and CoP nanosheets on the inside and outside surface of 3DOM g-C_3N_4 framework, respectively. And the rationality of spatial distribution positions for Au nanoparticles and CoP nanosheets on the surface of 3DOM g-C_3N_4 is systematically investigated. Additionally, to further enhance the charge transfer efficiency as well as the photocatalytic activity of CoP/3DOM g-C_3N_4/Au, we have also studied the effect of charge transfer distance (from the interior of g-C_3N_4 framework to the cocatalyst surface) on the photocatalytic performance by precisely controlling average wall thickness of 3DOM g-C_3N_4. As expected, the synergistic effect of dual cocatalysts with spatially separated positioning and optimal charge transfer distance significantly facilitates the charge transfer of CoP/3DOM g-C_3N_4/Au, thereby contributing to a remarkable apparent quantum efficiency and high photocatalytic H_2 evolution activity.

2. Experimental

2.1. Synthesis of 3D ordered SiO_2 and 3D ordered Au/SiO_2 with different average SiO_2 diameters

The 3D ordered Au/SiO_2 with different average SiO_2 diameters were prepared by the following method. Typically, 2 mL of aqueous ammonia and 2 mL of deionized water were dispersed in 15 mL of ethanol and vigorously stirred for 10 min at different temperatures, including 30 °C, 40 °C and 50 °C. A mixture of 2 mL of tetraethyl orthosilicate (TEOS) and 5 mL of ethanol was added dropwise to the above dispersion solution under magnetic stirring for 3.5 h to form SiO_2 nanospheres. It is noted that the control of reaction temperature for 30 °C, 40 °C and 50 °C can obtain SiO_2 nanospheres with the average diameters of 500 nm, 400 nm, 300 nm, respectively. Then, the tetrachloroauric acid hydrate ($AuCl_3 \cdot HCl \cdot 4H_2O$) was dissolved into the above reaction system with an Au loading of 1 wt%. After stirring for 30 min at the same temperature, 1 mL of alcoholic solution containing sodium borohydride ($NaBH_4$, 6 mg mL^{-1}) was added dropwise and kept for another 30 min to obtain Au nanoparticle/SiO_2 composites with different average SiO_2 diameters. Subsequently, the Au/SiO_2 composites were isolated, washed several times with deionized water and ethanol before ultrasonically re-dispersing in 15 mL of ethanol. Afterward, the 3D ordered Au/SiO_2 with different average SiO_2 diameters were obtained by centrifuging the above composites with a revolution speed of 2000 rpm/min for 3 h, and dried at 70 °C for 12 h. Then the 3D ordered products were calcinated at 650 °C for 6 h in N_2 to further improve the interconnection of 3D ordered structure. The obtained 3D ordered Au/SiO_2 samples with different average diameters of 300 nm, 400 nm and 500 nm were denoted as SA3, SA4 and SA5, respectively. As a reference, the pure 3D ordered SiO_2 with an average diameter of 400 nm (shorthand for S4) was prepared under the similar conditions of SA4, and the only difference is the sustained reaction for 4.5 h at 40 °C without the introduction of Au nanoparticles.

2.2. Synthesis of CoP/3DOM g-C_3N_4/Au with different average wall thicknesses

2 g of above 3D ordered Au/SiO_2 product (one of SA3, SA4 and SA5) was neutralized using a HCl solution (1 M), and dried at 70 °C for 12 h. Then, the product was impregnated in excessive melted cyanamide liquid (5 g) under vacuum atmosphere at 60 °C for 24 h. Whereafter, the g-C_3N_4/Au/SiO_2 composite was obtained by removing the superfluous cyanamide liquid and then calcining at 550 °C for 4 h in N_2 atmosphere with a heating rate of 2.3 °C min^{-1}. Moreover, the CoP/g-C_3N_4/Au/ SiO_2 composite was synthesized on the basis of the above preparation. 0.4 g of g-C_3N_4/Au/SiO_2 composite was mashed and dispersed in 20 mL of deionized water. Next, a certain amount of cobalt acetate was added

to the above dispersion solution with a Co loading of 5 wt% and vigorously stirred at room temperature for 3 h. Then, quantitative NaOH aqueous solution (0.2 M, a molar ratio of Co^{2+}:NaOH at 1:2) was added dropwise into the above mixed solution, and stirred for 1 h at same temperature. The precipitate was collected, washed several times with deionized water and ethanol, and dried at 70 °C for 12 h. According to the given atomic ratio of Co:P at 1:10, the above precipitate and NaH_2PO_2 were ground together and mixed uniformly, then heated to 300 °C for 4 h in N_2 atmosphere with a heating rate of 2 °C min^{-1}. After cooling to nature temperature, the final CoP/3DOM g-C_3N_4/Au was obtained by removing the SiO_2 with 5 wt% HF aqueous solution. Based on the different 3D ordered Au/SiO_2 templates of SA3, SA4 and SA5, the as-prepared CoP/3DOM g-C_3N_4/Au samples with different macropore diameters of 300 nm, 400 nm and 500 nm were denoted as ACC3, ACC4 and ACC5, respectively.

2.3. Synthesis of 3DOM g-C_3N_4, 3DOM g-C_3N_4/Au and CoP/3DOM g-C_3N_4

To better evaluate the performances of ACC series samples, three main reference samples of 3DOM g-C_3N_4, 3DOM g-C_3N_4/Au and CoP/ 3DOM g-C_3N_4 were synthesized using S4 or SA4 as a template. The synthesis of 3DOM g-C_3N_4 is as follows: The g-C_3N_4/SiO_2 composite was synthesized using S4 as the template under the similar conditions of the above g-C_3N_4/Au/SiO_2 composite. After immediately removing the SiO_2 template with 5 wt% HF aqueous solution, the 3DOM g-C_3N_4 was obtained and denoted as PCN. The 3DOM g-C_3N_4/Au sample was synthesized by removing the SA4 SiO_2 template of the above-mentioned g-C_3N_4/Au/SiO_2 composite with 5 wt% HF aqueous solution, and denoted as ACN. It is worth pointing out that the Au nanoparticles were anchored on the inside surface of the whole 3DOM g-C_3N_4 framework in the ACN sample. The CoP/3DOM g-C_3N_4 sample (CNC) was synthesized under the similar conditions of ACC4, and the only difference is choosing S4 as the template rather than SA4. It is noted that the CoP nanosheets were loaded on the outside surface of the whole 3DOM g-C_3N_4 framework in the CNC sample.

2.4. Synthesis of Au/3DOM g-C_3N_4, Au/3DOM g-C_3N_4/Au, CoP/3DOM g-C_3N_4/CoP, Au-CoP/3DOM g-C_3N_4/Au-CoP

In order to shed light on the spatial distribution position effect of Au and CoP in the 3DOM g-C_3N_4 framework, the samples of Au/3DOM g-C_3N_4, Au/3DOM g-C_3N_4/Au, CoP/3DOM g-C_3N_4/CoP and Au-CoP/ 3DOM g-C_3N_4/Au-CoP were prepared using S4 or SA4 as a template. As for the Au/3DOM g-C_3N_4 sample (shorthand for OCN), the Au nanoparticles were anchored on the outside surface of the whole 3DOM g-C_3N_4 framework. Its preparation procedure is as follows: The same amount of Au nanoparticles (an Au loading of 1 wt%) was deposited on the above-mentioned g-C_3N_4/SiO_2 composite using the same reduction method of $NaBH_4$, and Au nanoparticles were selectively deposited on the outside surface of the whole 3DOM g-C_3N_4 framework. After removing the SiO_2 template with 5 wt% HF aqueous solution, the Au/ 3DOM g-C_3N_4 was obtained. In regard to the Au/3DOM g-C_3N_4/Au sample (shorthand for WCN), the Au nanoparticles were anchored both on the inside and outside surface of the whole 3DOM g-C_3N_4 framework. And the WCN sample was prepared by the photodeposition method using the 3DOM g-C_3N_4 as the precursor. Typically, before the photocatalytic hydrogen evolution reaction, a certain amount of $AuCl_3 \cdot HCl \cdot 4H_2O$ was dissolved to the reaction system containing 3DOM g-C_3N_4 with an Au loading of 1 wt%, then photoreduced into Au nanoparticles that were uniformly anchored both on the inside and outside surface of 3DOM g-C_3N_4 framework. As for the CoP/3DOM g-C_3N_4/ CoP sample (shorthand for CNG), the CoP nanosheets were loaded both on the inside and outside surface of the whole 3DOM g-C_3N_4 framework. The CNG sample was synthesized by loading same amount of CoP (a Co loading of 5 wt%) on the above 3DOM g-C_3N_4 sample under the

similar conditions of CNC. In terms of the Au-CoP/3DOM g-C$_3$N$_4$/Au-CoP sample (shorthand for WCCG), Au and CoP were randomly distributed on the inside and outside surface of the whole 3DOM g-C$_3$N$_4$ framework. The WCCG was synthesized by photodepositing same amount of Au nanoparticles on the CNG sample using the above-mentioned method.

2.5. Characterization

The crystal phase of obtained samples was characterized relying on an X-ray diffraction (XRD, Lab X XRD-6100, SHIMADZU). The morphology and microstructure of products were investigated using a transmission electron microscopy (TEM, JEM-2100, JEOL) and a field-emission scanning electron microscope (FE-SEM, JSM-6700 F, JEOL) equipped with an energy dispersive X-ray spectroscopy (EDX). The element composition of as-prepared samples was analyzed by an X-ray photoelectron spectroscopy apparatus (XPS, AXIS ULtrabld) and an inductively coupled plasma mass spectrometer (ICP-MS, NexION™ 350D, PerkinElmer). The ultraviolet-visible diffuse reflectance spectra (DRS) were recorded by a UV–vis spectrophotometer (UV-2600, SHIMADZU). The BET specific surface areas were obtained using an advanced automatic BET analyzer (Autosorb-iQ-TPX, Auantachrome). The photoluminescence emission spectra (PL) and fluorescence decay spectra were collected on a luminescence spectrophotometer (FLS980, Edinburgh Instruments) with a 340 nm excitation wavelength.

2.6. Photocatalytic activity measurement

The photocatalytic H$_2$ production was carried out using a gas-closed system with an outer Pyrex reaction cell (100 mL). Briefly, 50 mg of photocatalyst powder was dispersed into 50 mL of deionized water containing 10 mL of triethanolamine as the sacrificial electron donor. Before the reaction, the reaction system was deaerated using the bubbled treatment with high purity nitrogen to drive away the air. Then the reaction was performed under a 300 W Xenon lamp illumination (HSX-F300, NbeT) equipped with a 420 nm UV-cutoff filter. The evolved H$_2$ was detected on a gas chromatograph (SP-2100 A, Beifen-Ruili) with a 5 Å molecular sieve column and a TCD detector. The apparent quantum efficiency (AQE) for the as-prepared samples was measured under the same reaction conditions except by replacing the 420 UV-cutoff filter with a band-pass interference filter centered at 375, 435, 475, 550 and 700 nm, respectively. The average hydrogen evolution rate was tested after illumination for 3 h.

2.7. Photoelectrochemical measurement

The transient photocurrent response and electrochemical impedance spectroscopy (EIS) of resulting products were measured by an electrochemical working station (PMC-1000/DC, AMETEK) with a standard three-electrode system. In the system, the Ag/AgCl electrode, platinum wire and glassy carbon electrodes coated by as-prepared photocatalysts were served as the reference electrode, counter electrode and working electrodes, respectively. A Na$_2$SO$_4$ aqueous solution of 1 M was chosen as the electrolyte.

3. Results

Fig. 1 schematically illustrates the overall synthetic approach of CoP/3DOM g-C$_3$N$_4$/Au nanocomposite. Firstly, the SiO$_2$ nanospheres with different average diameters were synthesized by controlling the reaction temperatures (30 °C, 40 °C and 50 °C, respectively) using a modified Stöber's method [16]. Soon afterwards, owing to the electrostatic attraction effect, the cation of Au^{3+} can be readily loaded on the surface of negatively charged SiO$_2$ nanospheres and then reduced to Au nanoparticles, which uniformly anchored on entire SiO$_2$ surface to form the Au/SiO$_2$ composite. Next, the formed composite can be self-

assembled to obtain the 3D ordered Au/SiO$_2$ through a centrifugation method, and further heated at 650 °C in N$_2$ atmosphere to improve the interconnection of 3D ordered nanostructure. After that, massive cyanamide (CA) molecules were continually filled into the interstices of 3D ordered Au/SiO$_2$ framework neutralized by HCl under vacuum atmosphere to form the CA/Au/SiO$_2$ hybrid, which can be conveniently converted into the g-C$_3$N$_4$/Au/SiO$_2$ composite via self-condensation of CA at 550 °C. It is noteworthy that Au nanoparticles can be estranged from the neutralized SiO$_2$ and easily interacted with CA due to the presence of amidogen in the CA molecules, and then fixed on the inside surface of g-C$_3$N$_4$ framework through the subsequent high-temperature calcination treatment. Thereafter, the cation of Co^{2+} was selectively absorbed on the outside surface of negatively charged g-C$_3$N$_4$ framework and then convert into Co(OH)$_2$ under alkaline condition, which next was transformed into CoP nanosheets assembled on the outside surface of g-C$_3$N$_4$ framework by the heating reaction with NaH$_2$PO$_2$ in 300 °C. After removing the SiO$_2$ with HF aqueous solution (5 wt%), the resulting 3DOM g-C$_3$N$_4$ with spatially separated dual cocatalysts of Au and CoP (ACC) was thus obtained in this way.

The X-ray diffraction (XRD) patterns of 3DOM g-C$_3$N$_4$ (PCN), 3DOM g-C$_3$N$_4$/Au (ACN), CoP/3DOM g-C$_3$N$_4$ (CNC) and ACC series samples are displayed in Fig. 2a, and the XRD profiles of PCN and ACN samples present a typical peak at around 27.2°, corresponding to the (002) crystal plane of periodic melon networks (JCPDS #87-1526), strongly proving the presence of g-C$_3$N$_4$ [21]. An obvious shift from 27.2° to 27.7° for the (002) peak of g-C$_3$N$_4$ occurs in the patterns of CNC and ACC series samples, which may be due to the effect of CoP loading [22]. With respect to ACN and ACC series samples, four strong characteristic peaks (38.3°, 44.5°, 64.7° and 77.7°) can be easily found and belonged to the crystal structure of Au (JCPDS #04-0784). To better observe the diffraction peaks of CoP, the local magnification XRD patterns of CNC, ACC3, ACC4 and ACC5 are shown in Fig. 2b. It can be found that, except for the two prominent peaks of Au (38.3° and 44.5°), all the other peaks are well conformed to the crystal planes of CoP (JCPDS #29-0497). Furthermore, to gain deeper insight into the surface chemical environment and element composition of 3DOM g-C$_3$N$_4$ with the loading of Au and CoP, the X-ray photoelectron spectroscopy (XPS) measurement for ACC4 sample was performed. As shown in Fig. 2c, the C 1 s region indicates the presence of C−C in aromatic rings at 284.8 eV, N−C=N at 286.3 eV and C−NH$_2$ at 288.4 eV, thereby revealing the formation of g-C$_3$N$_4$ nanocrystal [23]. The N 1 s region (Fig. 2d) suggests the presence of the sp^2-hybridized nitrogen in C−N=C at 398.6 eV, tertiary nitrogen in N−(C)$_3$ groups at 400.0 eV, terminal amino-groups (-NH$_2$) at 401.2 eV, and the small peak at the binding energy of 404.5 eV is due to the charging effects in heterocycles of g-C$_3$N$_4$ [24–26]. The above chemical bonds in C 1 s and N 1 s regions together constitute the basic structural units of g-C$_3$N$_4$ organic polymer. The Au 4f region (Fig. 2e) can be fitted into three peaks: The two major ones at 82.3 eV and 86.1 eV are in accordance with Au 4f$_{7/2}$ and Au 4f$_{5/2}$ of metallic Au (Au°), respectively [27,28], the minor one at 83.1 eV is assigned to Au (III) oxidation state, probably due to the interaction of Au nanoparticles and O$_2$ in air under high-temperature condition during the synthetic process of ACC sample [28]. In Fig. 2f, the Co 2p region shows two peaks at 778.5 eV and 795.3 eV, which are corresponded to Co 2p$_{3/2}$ and Co 2p$_{1/2}$ in CoP [29], and the P 2p region reveals the presence of P 2p$_{1/2}$ in CoP at 129.6 eV and oxidized P species at 133.2 eV [22,29]. Additionally, the element content of cocatalysts over different samples was measured by an inductively coupled plasma mass spectrometer (ICP-MS). As displayed in Table S1, ACN and ACC series samples show the close element content of Au, while CNC and ACC series samples have the similar element content of Co and P, these strongly indicate that the very close amounts of Au and CoP cocatalysts have been successfully introduced into the corresponding samples.

Fig. 3 shows the morphologies of 3D ordered Au/SiO$_2$ templates with different average SiO$_2$ diameters (SA3, SA4 and SA5). As seen in
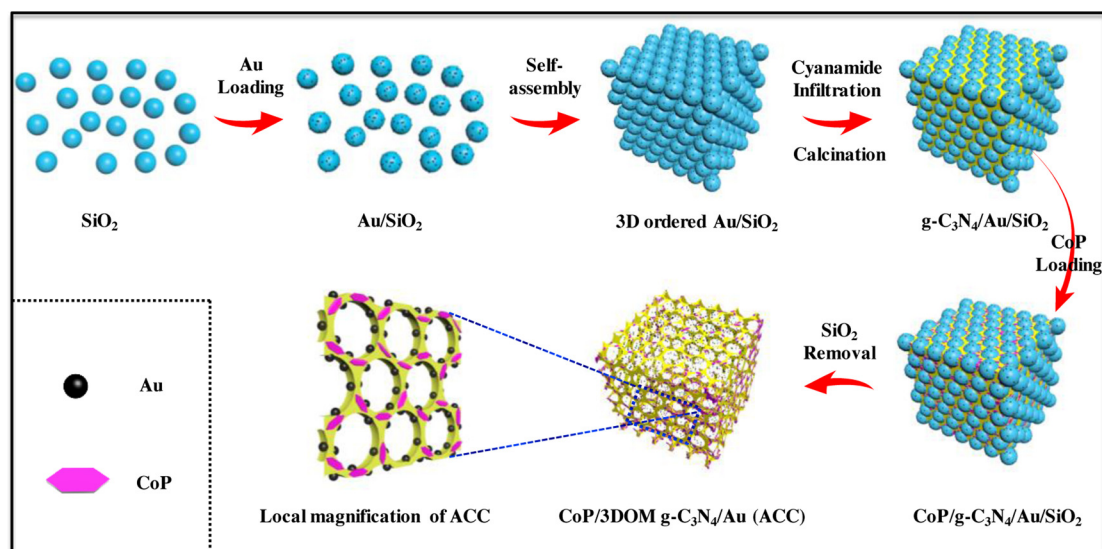
Fig. 1. Schematic illustration of the formation procedure for CoP/3DOM g-C$_3$N$_4$/Au (ACC).

Fig. 3a, the large-scale SEM image of SA3 shows that numerous closely packed Au/SiO$_2$ nanospheres were assembled to form the three-dimensional periodic orderd array structure. From the magnification SEM image of SA3 (inset in Fig. 3a), it can be found that lots of Au nanoparticles are uniformly loaded on the individual SiO$_2$ nanosphere. Meanwhile, the TEM image in Fig. 3d shows that individual SiO$_2$ nanosphere possesses an average diameter of 300 nm (SA3). In addition, similar information can be gained from Fig. 3b,c and their insets, it is observed that the SA4 and SA5 have an average SiO$_2$ diameter of 400 nm and 500 nm, respectively (Fig. 3e,f). Fig. 3g–i show the corresponding schematic diagrams of Au/SiO$_2$ nanospheres with different average diameters, which clearly demonstrate the gradually increasing trend of average SiO$_2$ diameter from SA3 to SA4, then to SA5.

The morphologies of PCN, ACN and CNC reference samples were also characterized. As shown in Fig. 4a,d, the PCN sample presents an opened-up, well-defined interconnected macroporous structure with an average macropore diameter of 400 nm, and massive mesopores and

micropores are formed on the framework of 3DOM g-C$_3$N$_4$. In Fig. 4b,e, the ACN reference sample reveals that numerous Au nanoparticles were anchored on the inside surface of 3DOM g-C$_3$N$_4$ framework with a macropore diameter of avg. 400 nm, while the CNC sample (Fig. 4c,f) presents the similar macroporous structure and uniformly distributed CoP nanosheets on the outside surface of g-C$_3$N$_4$ framework.

Fig. 5 shows the nanostructures of the spatially separated Au/3DOM g-C$_3$N$_4$/CoP samples. From the large-scale SEM images (Fig. 5a–c), it can be found that the three as-prepared samples show highly ordered 3DOM structure with a pore diameter of avg. 300 nm (ACC3), avg. 400 nm (ACC4) and avg. 500 nm (ACC5), respectively, which are derived from the SA-series templates with different average SiO$_2$ diameters (Fig. 3). Due to the formation of macroporous structure, the incident light can easily penetrate into the inside of 3DOM framework and excite the Au nanoparticles to produce the hot electrons during the photocatalytic reaction of H$_2$ production. The magnification SEM (Fig. 5d–f) and TEM (Fig. 5g–i) images further indicate that massive
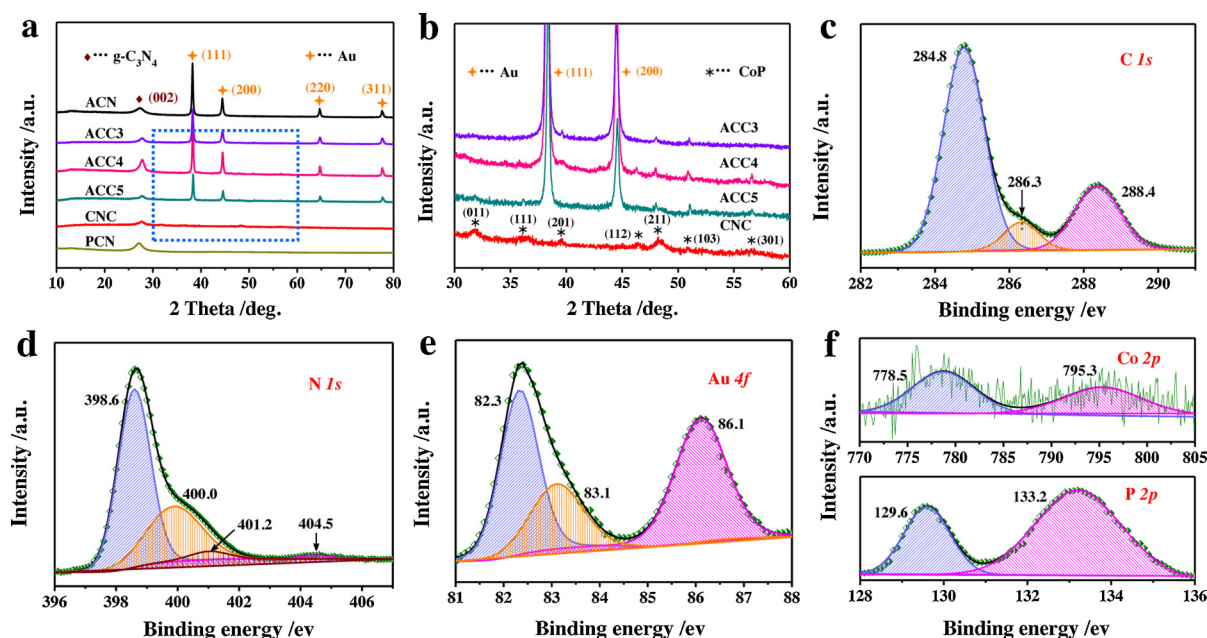

Fig. 2. a) XRD patterns of as-fabricated samples. b) The local magnification XRD patterns of CNC, ACC3, ACC4 and ACC5. XPS spectra of ACC4 in the regions of c) C 1 s, d) N 1 s, e) Au 4f, f) Co 2p and P 2p.
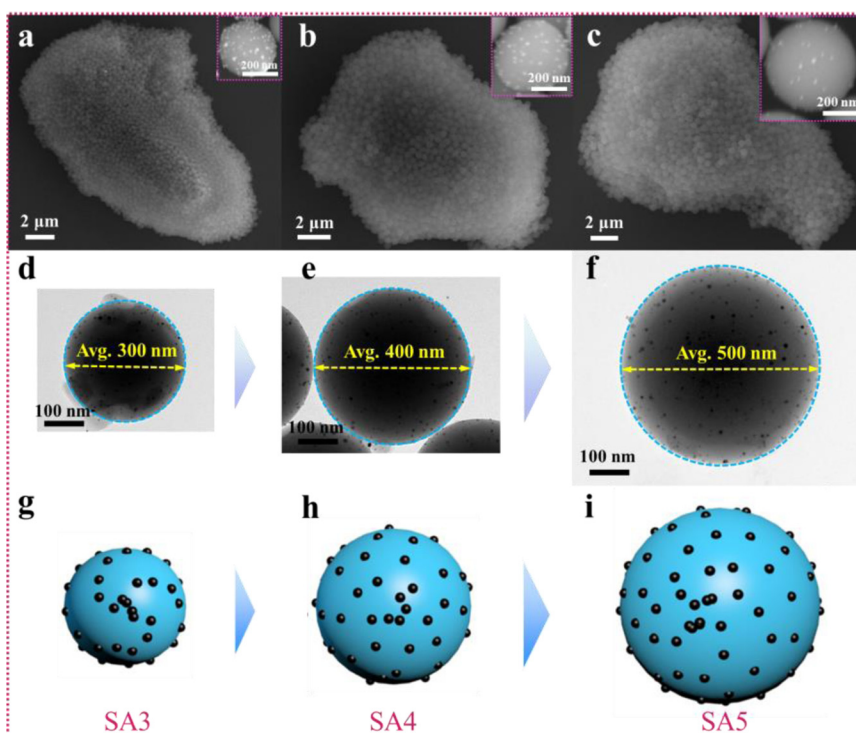
Fig. 3. SEM images of a) SA3, b) SA4 and c) SA5. Magnification SEM images of (inset in a) SA3, (inset in b) SA4 and (inset in c) SA5. TEM images of d) SA3, e) SA4 and f) SA5. The corresponding schematic diagrams of g) SA3, h) SA4 and i) SA5.

well-dispersed CoP nanosheets with an average length of 15 nm and an average width of 10 nm were uniformly loaded on the partial outside-surface of g-C$_3$N$_4$ framework, suggesting that the CoP has been successfully introduced in the pre-designed spatial position of 3DOM framework. As for ACC3 (Fig. 5d,g), both the SEM and TEM images clearly show that the average wall thickness between two adjacent macropores in 3DOM g-C$_3$N$_4$ framework (Fig. 5j) is 40 nm. Similarly, ACC4 (Fig. 5e,h,k) and ACC5 (Fig. 5f,i,l) also show an average wall thickness of 80 nm and 120 nm, respectively. All of the aforementioned electron microscope results indicate that we have successfully constructed the Au/3DOM g-C$_3$N$_4$/CoP ternary nanocomposites with different average wall thicknesses, achieving the expected goal for the synthesis of CoP/3DOM g-C$_3$N$_4$/Au with different charge transfer distances.

To further shed light on the unique structure of 3DOM g-C$_3$N$_4$ with spatially separated dual cocatalysts of Au and CoP, the local magnification TEM and HR-TEM images of ACC4 are exhibited in Fig. 6. As shown in Fig. 6a,b, noted that Au nanoparticles (avg. size of 5 nm) and CoP nanosheets (avg. length of 15 nm and avg. width of 10 nm) can be effectively controlled to grow separately on the inside surface and outside surface of 3DOM g-C$_3$N$_4$ framework, as evidenced by the TEM observations of ACN and CNC in Fig. 4. The HR-TEM images of ACC4 (Fig. 6c,d) strongly confirm the presence of dual cocatalysts with spatially separated positions, where the lattice-fringe spacing of 0.28 nm (Fig. 6c) and 0.20 nm (Fig. 6d) are indexed to the (011) lattice plane of CoP (JCPDS #29-0497) and the (200) lattice plane of Au (JCPDS #04-0784), respectively [30]. Additionally, the elemental mappings (Fig. S1) and energy-dispersive X-ray images (EDX, Fig. S2) of ACC4 further prove the presence of dual cocatalysts (Au and CoP) with the spatially
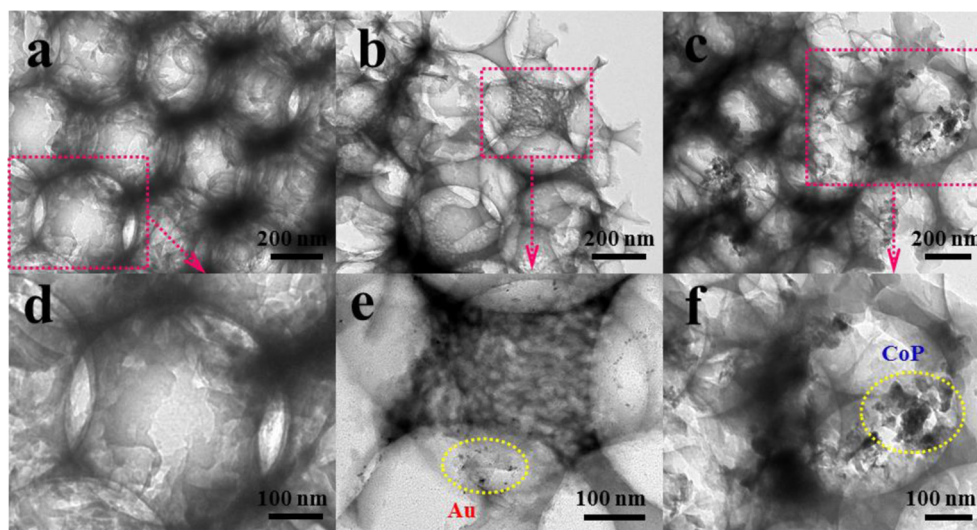

Fig. 4. TEM images of a) PCN, b) ACN and c) CNC. The local magnification TEM images of d) PCN, e) ACN and f) CNC.
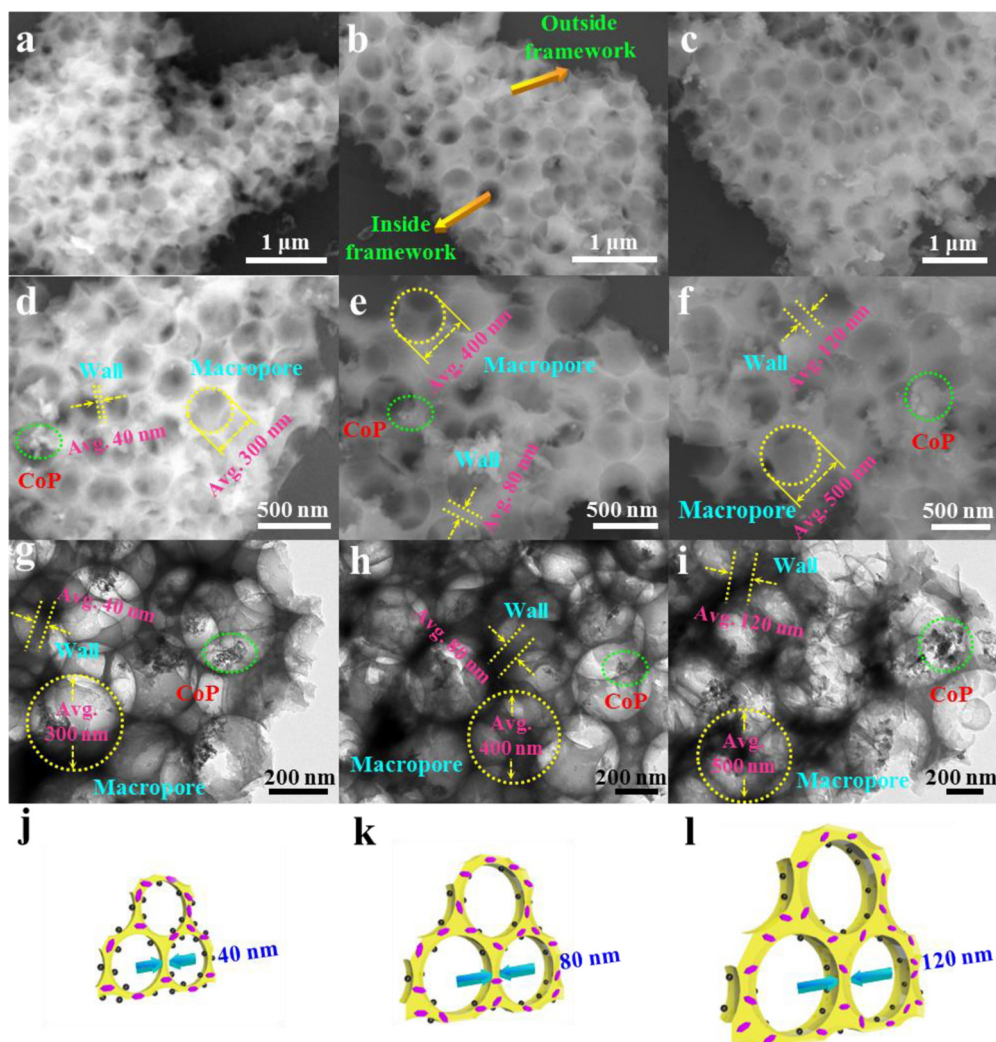
Fig. 5. SEM images of a) ACC3, b) ACC4 and c) ACC5. Magnification SEM images of d) ACC3, e) ACC4 and f) ACC5. TEM images of g) ACC3, h) ACC4 and i) ACC5. The corresponding schematic diagrams of j) ACC3, k) ACC4 and l) ACC5.

separated positioning in 3DOM g-C_3N_4 framework.

Time-dependent photoinduced H_2 generation over various samples was evaluated using triethanolamine as the sacrificial reagent under visible-light illumination ($\lambda > 420\,nm$). As illustrated in Fig. 7a,b, with 3DOM g-C_3N_4 alone (PCN), a negligible amount of H_2 (19.1 μmol h^{-1} g^{-1}) can be produced, due to its considerably inferior charge transfer capacity. Incredibly, with the loading of Au nanoparticles on the inside surface of 3DOM g-C_3N_4 framework, ACN sample with the optimal Au-loading amount of 1 wt% displays a sharply increased hydrogen-evolution rate (HER) of 2127.5 μmol h^{-1} g^{-1} (Fig. S3), nearly 111.4 times higher than that of PCN. Similarly, accompanied by the loading of CoP nanosheets on the outside surface of 3DOM g-C_3N_4 framework, CNC sample with the optimal CoP-loading amount of 5 wt% (Fig. S4) shows an excellent HER activity of 1805.5 μmol h^{-1} g^{-1}, exceeding PCN by a factor of 94.5. These above results strongly indicate the attractive cocatalyst-induced properties in the photocatalytic H_2 evolution. As expected, the spatially separated Au/3DOM g-C_3N_4/CoP series samples show remarkable H_2 evolution performances. It can be seen that the ACC4 sample (a wall thickness of avg. 80 nm) presents the highest HER of 11,820.1 μmol h^{-1} g^{-1}, much higher than that of ACC3 (a wall thickness of avg. 40 nm, 7960.7 μmol h^{-1} g^{-1}) and ACC5 (a wall thickness of avg. 120 nm, 4938.5 μmol h^{-1} g^{-1}), up to 619.9, 6.5 and 5.6 times by contrast with that of PCN, CNC and ACN sample, respectively. According to the above results, it is rational to propose that the combined effect of 3DOM g-

C_3N_4 architecture, dual cocatalysts with spatially separated positioning and optimal charge transfer distance (a corresponding wall thickness of avg. 80 nm) would significantly improve the photocatalytic H_2 generation activity.

Fig. 7c shows the stability performance of the ACC series samples. As shown in Fig. 7c, after five cycling tests, the ACC3 sample exhibits a sharply decreased activity of H_2 generation (only 28.9% of initial HER value), this is due to its relatively fragile framework with a thin wall thickness of avg. 40 nm. Wondrously, both ACC4 (a wall thickness of avg. 80 nm) and ACC5 (a wall thickness of avg. 120 nm) samples remain the stable H_2 generation activity by contrast with their respective initial HER values, indicating the excellent stablity and reusability of the two samples. Fig. S5 shows the TEM images of the CoP/3DOM g-C_3N_4/Au series samples obtained after the recycled tests: It can be easily found that ACC3 shows a severely damaged 3DOM structure, while both ACC4 and ACC5 keep a relatively intact 3DOM architecture. Moreover, no obvious differences of XRD patterns can be observed from the fresh ACC4 sample and recycled ACC4 sample (Fig. S6). These all manifest that ACC4 sample with the optimal charge transfer distance owns outstanding H_2 evolution activity and stability, and this kind of novel nanostructured photocatalyst would be a promising candidate for solar-driven hydrogen generation.

The apparent quantum efficiency (AQE) of H_2 generation over the ACC series samples was measured under different monochromatic incident lights. As illustrated in Fig. 8, all the samples show the similar
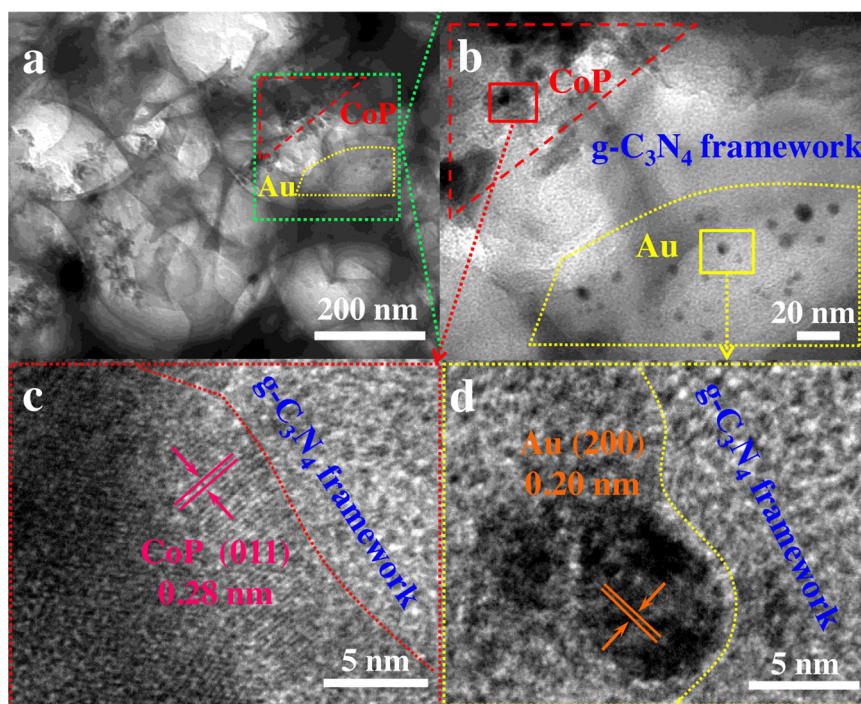
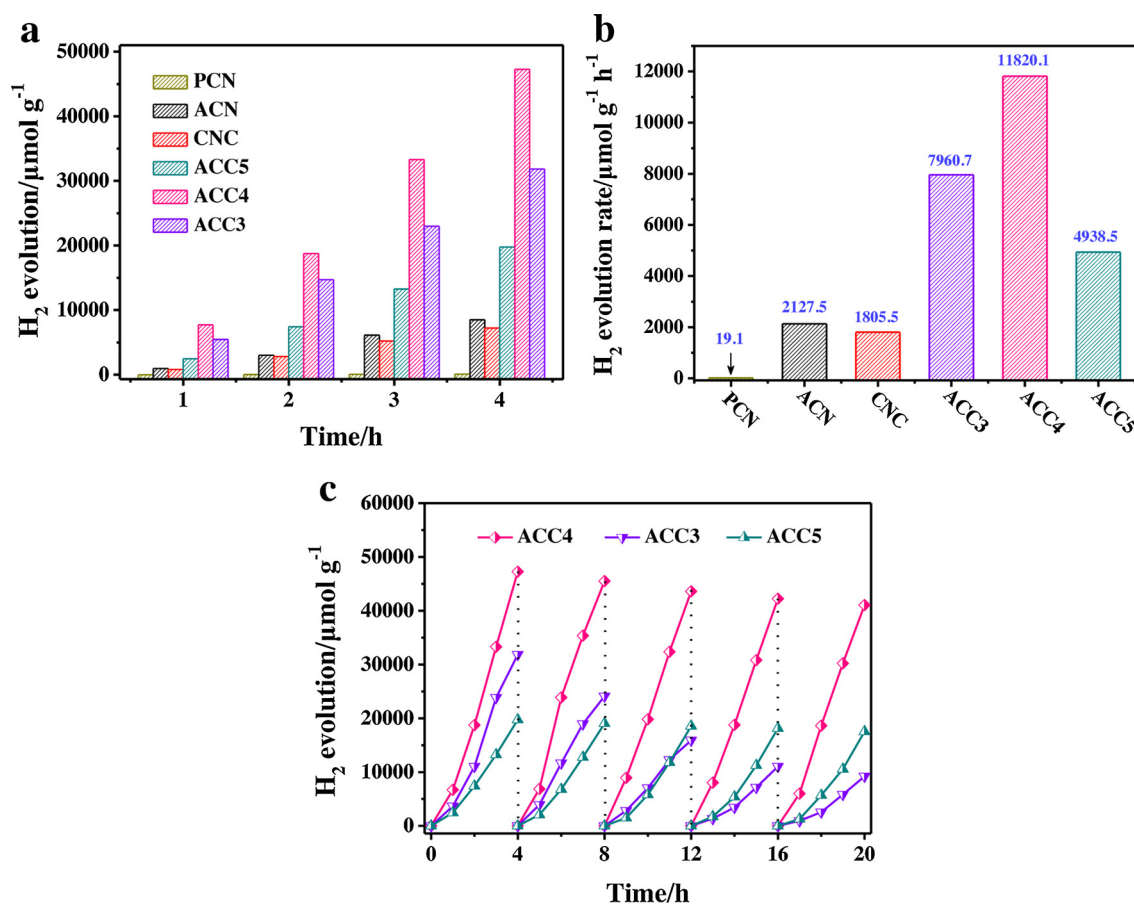**Fig. 6.** a, b) The local magnification TEM images of ACC4. c, d) HR-TEM images of ACC4.

Fig. 7. a) Time-dependent photocatalytic H_2 evolution and b) Hydrogen-evolution rate over ACC series samples and their main reference samples under visible-light illumination ($\lambda > 420$ nm). c) Recycle tests of photocatalytic H_2 evolution over ACC3, ACC4 and ACC5 under visible-light illumination ($\lambda > 420$ nm).
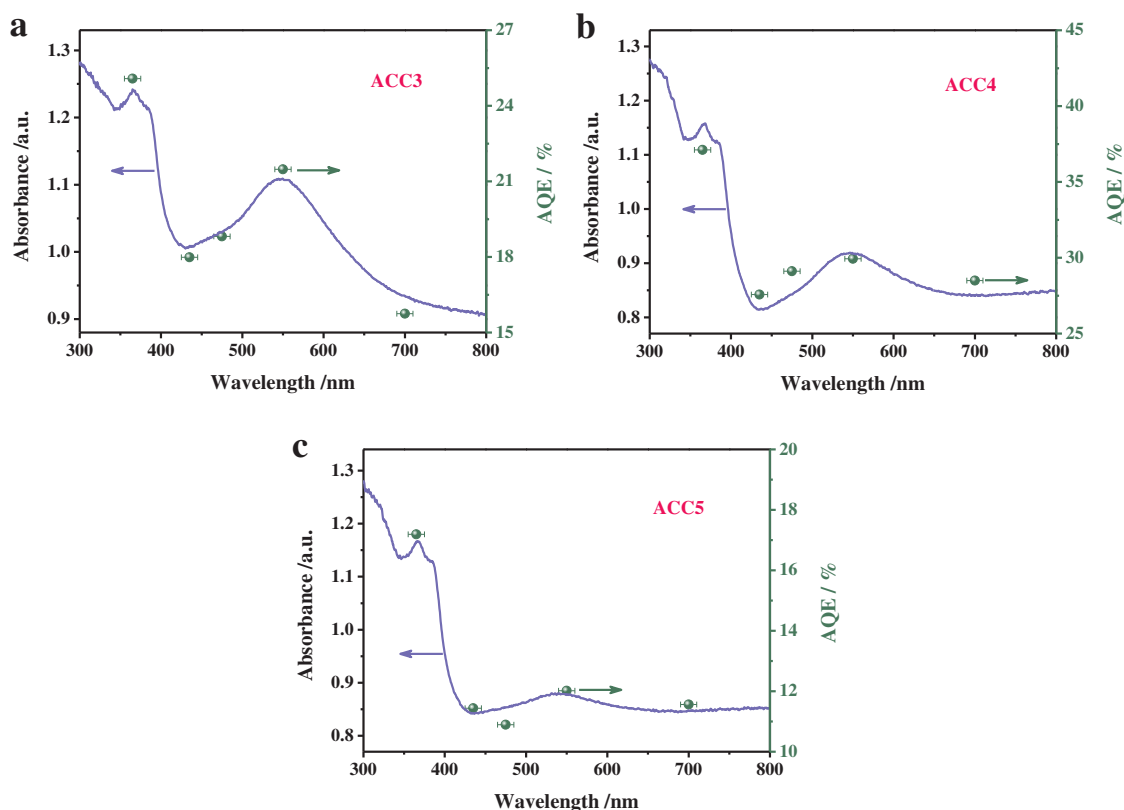
Fig. 8. Wavelength-dependent AQE for photocatalytic H_2 evolution over a) ACC3, b) ACC4 and c) ACC5.

wavelength-dependent trend of AQE that is closely followed the absorption spectrum of UV–vis diffuse reflectance spectra (DRS). Differing from the majority of g-C_3N_4 photocatalysts, which usually present a continuously declined trend of AQE as a function of the increased wavelength in the 400–800 nm region [31,32], a significant increase of AQE value respectively occurs at 550 nm and 700 nm in the ACC series samples owing to the strong photoabsorption in the 430–700 nm region induced by the surface plasmon resonance (SPR) effect of Au nanoparticles, and this SPR process can generate lots of hot electrons to enhance the photocatalytic H_2 evolution [33–36]. Notably, the AQE of ACC3 for HER at 365, 435, 550 and 700 nm was as high as 25.1%, 18.0%, 21.5% and 15.8% (Fig. 8a), respectively, indicative of the advantages of spatially separated dual cocatalysts. Additionally, ACC5 still has an excellent AQE at 365, 435, 550 and 700 nm of 17.2%, 11.4%, 12.0% and 11.6% (Fig. 8c), respectively. More importantly, the ACC4 sample with the optimal charge transfer distance shows the highest AQE at 365, 435, 550 and 700 nm of 37.1%, 27.6%, 29.9% and 28.5% (Fig. 8b), respectively, gaining entry to the ranks of best photocatalytic H_2 evolution activities for g-C_3N_4 candidates, especially in the AQE at 550 nm that has achieved a leading position, again evidencing the remarkable H_2 evolution performance endowed by the spatial positioning effect of dual cocatalysts and optimal charge transfer distance.

The optical properties of as-prepared samples were investigated by UV–vis DRS. As displayed in Fig. 9a, PCN shows routine visible-light absorption ability centered on 380–700 nm. With respect to CNC, a dramatically enhanced visible-light harvesting presents in its spectrum, this is due to the intrinsic light-absorption property of CoP nanosheets anchored on the outside surface of g-C_3N_4 framework [15]. Of note, ACN shows an enhancement of visible-light absorption by contrast with PCN, and exhibits a remarkable absorption peak at 550 nm, due to the above-mentioned SPR effect of Au nanoparticles [27,33]. Similarly to ACN, all the ACC series samples show strong visible-light absorption spectra with a SPR characteristic peak due to the synthetic effect of Au

and CoP loading, and the visible-light absorption intensity is gradually increased along with the diminution of average macropore diameter (from ACC5 to ACC4, then to ACC3), probably due to the gradually increased multiple scattering effect of 3DOM architecture [37,38]. The N_2 adsorption-desorption isotherms of different samples were also measured. As shown in Fig. 9b, a typical type-IV isotherm featured with the type H3 hysteresis loop in 0.8–1.0 relative pressure (p/p_0) can be clearly observed in all profiles, indicative of the presence of numerous mesopores and macropores [39,40]. The textural properties of different samples are exhibited in Table S2. The PCN (12.79 $m^2 g^{-1}$, 0.09 $cm^3 g^{-1}$) and CNC (12.43 $m^2 g^{-1}$, 0.07 $cm^3 g^{-1}$) possess the very closed specific surface area (S_{BET}) and pore volume, while ACN shows the enhanced S_{BET} value (20.02 $m^2 g^{-1}$) and pore volume (0.19 $cm^3 g^{-1}$) due to the introduction of many Au nanoparticles in the 3DOM structure [41,42]. In comparison with PCN, the ACC series samples display the increased S_{BET} and pore volume (32.08 $m^2 g^{-1}$ and 0.23 $cm^3 g^{-1}$ for ACC3, 24.59 $m^2 g^{-1}$ and 0.18 $cm^3 g^{-1}$ for ACC4, 19.05 $m^2 g^{-1}$ and 0.11 $cm^3 g^{-1}$ for ACC5), and the differences of S_{BET} and pore volume for these ACC series samples are derived from their different average macropore diameters.

Fig. 9c shows the photoluminescence (PL) spectra of different samples. A strong and broad emission peak can be found in the spectrum of PCN, manifesting a fairly high charge recombination rate of the single 3DOM g-C_3N_4 [14]. When single cocatalyst (Au or CoP) was loaded on the inside or outside surface of 3DOM g-C_3N_4 framework, the PL fluorescence of ACN or CNC was partially quenched, indicating a promotion of photoinduced charge transfer to a certain extent [43]. It is amazing that the ACC series samples exhibit much lower fluorescence intensity than PCN, ACN and CNC, suggesting the huge advantages of spatially separated dual cocatalysts on charge transfer. Particularly, ACC4 sample shows the lowest fluorescence intensity among all ACC series samples, furhter strongly supporting the importance of appropriate charge transfer distance. These charge separation results are proved again by the following transient photocurrent response tests
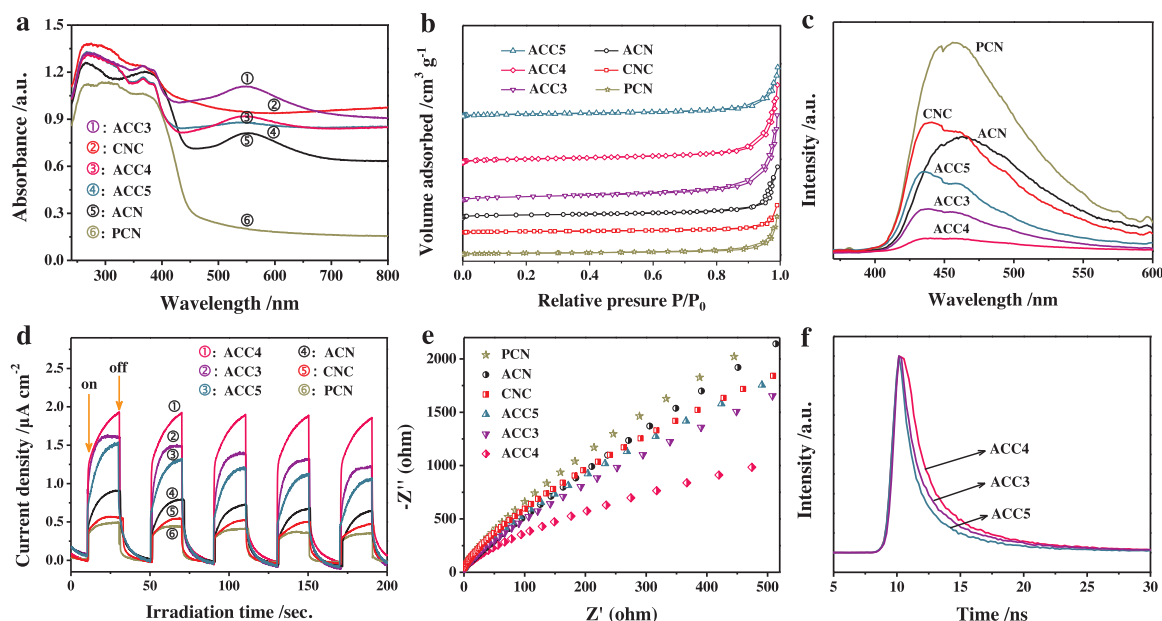
Fig. 9. a) UV–vis DRS, b) N_2 adsorption-desorption isotherms, c) Photoluminescence (PL) spectra, d) Transient photocurrent responses and e) EIS Nyquist plots for different samples. f) Fluorescence decay spectra for ACC3, ACC4 and ACC5.

(Fig. 9d) and electrochemical impedance spectroscopy (EIS, Fig. 9e). Notably, ACC4 sample show the highest photocurrent density in Fig. 9d, while it exhibits the smallest radius of Nyquist circle in Fig. 9e, both suggesting that ACC4 sample has the most excellent charge transfer capacity [44,45]. Additionally, the fluorescence decay spectra of ACC3, ACC4 and ACC5 were collected to further study the charge transfer dynamics process. As exhibited in Fig. 9f, all fluorescence spectra show an exponential intensity decay. In particular, ACC3 exhibits a slower decay kinetics by contrast with ACC5, and ACC4 has the slowest one among the three samples. Three fitting fluorescence lifetimes and corresponding amplitudes are listed in Table S3. All the shortest lifetime (τ_1), medium lifetime (τ_2) and longest lifetime (τ_3) of charge carriers maintain a gradually increased trend from ACC5 ($\tau_1 = 0.99$ ns, $\tau_2 = 4.51$ ns, $\tau_3 = 23.47$ ns) to ACC3 ($\tau_1 = 1.15$ ns, $\tau_2 = 4.93$ ns, $\tau_3 = 25.84$ ns), then to ACC4 ($\tau_1 = 1.36$ ns, $\tau_2 = 6.03$ ns, $\tau_3 = 28.78$ ns), and ACC4 sample owns the longest charge carrier lifetimes of τ_1, τ_2 and τ_3. These results strongly evidence that the well-designed Au/3DOM g-C_3N_4/CoP sample with the spatial positioning effect of dual cocatalysts and optimal charge transfer distance (ACC4) has acquired the maximization of charge transfer, thereby contributing to a significantly prolonged radiative lifetime of charge carriers [46–48].

4. Discussion

On basis of all the above characterization results, it is well concluded that the outstanding photocatalytic H_2 evolution activity of CoP/3DOM g-C_3N_4/Au (ACC) is closely related to the unique spatial positioning effect of dual cocatalysts (inside Au and outside CoP). In order to verify the correlation between spatial positioning effect of dual cocatalysts and photocatalytic H_2 evolution activity, a series of 3DOM g-C_3N_4 reference samples that loaded the single cocatalyst (Au or CoP) with different spatial distribution positions as well as the randomly distributed dual cocatalysts of Au and CoP on the 3DOM g-C_3N_4 framework were prepared. Fig. 10a,b shows the photocatalytic activity of H_2 evolution over different reference samples under visible-light illumination ($\lambda > 420$ nm). In comparison with the ACN sample that Au nanoparticles loaded on the inside surface of 3DOM g-C_3N_4 framework (Fig. S7a, 2127.5 μmol h^{-1} g^{-1}), the HER value of OCN sample (Au nanoparticles loaded on the outside surface of 3DOM g-C_3N_4

framework, Fig. S7b) turns out to be dramatically reduced (713.8 μmol h^{-1} g^{-1}), additionally, when the Au nanoparticles were randomly distributed on the internal and external surface of 3DOM g-C_3N_4, the as-obtained sample (WCN, Fig. S7c) also shows a low HER of 789.3 μmol h^{-1} g^{-1}. These phenomena strongly evidence that the rational loading of Au nanoparticles on the inside surface of 3DOM g-C_3N_4 framework is favorable for the improvement of photocatalytic H_2 evolution activity. Moreover, by contrast with the CNC sample that CoP nanosheets loaded on the outside surface of 3DOM g-C_3N_4 framework (Fig. S7d, 1805.5 μmol h^{-1} g^{-1}), the CNG sample that CoP nanosheets were loaded both on the inside and outside surface of 3DOM g-C_3N_4 framework (Fig. S7e), shows a decreased HER activity (1436.5 μmol h^{-1} g^{-1}), indicating that loading CoP nanosheets on the outside surface of 3DOM g-C_3N_4 framework can efficiently promote the visible-light-driven HER activity. Furthermore, the reference sample with randomly distributed Au and CoP on the whole framework of 3DOM g-C_3N_4 was synthesized (WCCG, Fig. S7f), and it displays a HER of 2533.2 μmol h^{-1} g^{-1}, which is only 21.4% of H_2 evolution amount of ACC4 (11,820.1 μmol h^{-1} g^{-1}). From the above HER results of these reference samples, it can be concluded that the optimal spatial positioning of Au and CoP in the 3DOM g-C_3N_4 framework significantly influences the photocatalytic H_2 evolution performance.

To further shed light on how the spatial positioning effect of dual cocatalysts exerts an influence on the photocatalytic H_2 evolution activity of the ACC samples, firstly, the visible-light absorption capacity of the reference samples is investigated and discussed. As shown in Fig. 10c, in comparison with ACN, WCN shows a sharply decreased SPR peak intensity at 550 nm, and when the single Au cocatalyst was completely loaded on the outside surface of 3DOM g-C_3N_4 framework (OCN), the above peak was virtually disappeared. This phenomena reveal that loading Au on the inside surface of 3DOM framework is beneficial for the visible-light absorption because the multiple scattering occured in the inside of 3DOM architecture could obviously improve the SPR effect of Au. Similarly, the CNG sample shows a much lower visible-light absorption than CNC, suggesting that loading CoP cocatalyst on the outside surface of 3DOM framework can facilitate the visible-light harvesting due to the more sufficient contact with light. As expected, when Au nanoparticles and CoP nanosheets were separately loaded on the inside and outside surface of 3DOM g-C_3N_4 framework, the ACC4 sample shows a strong visible-light absorption. These results
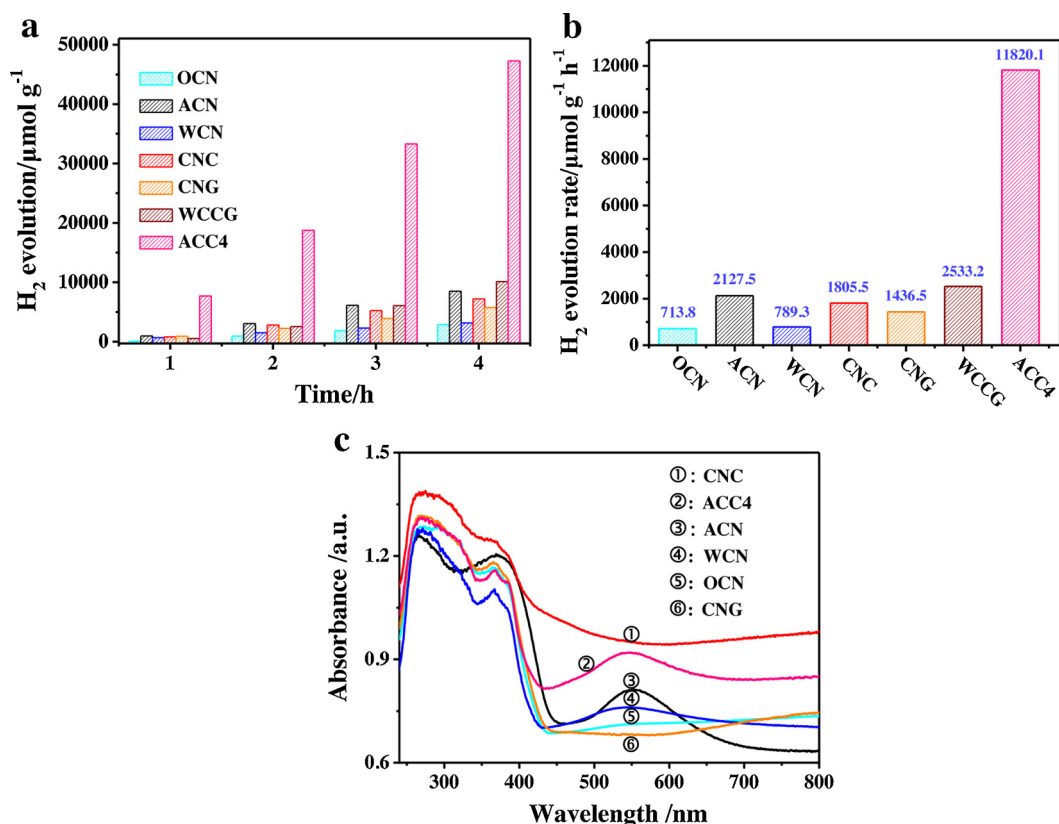
Fig. 10. a) Time-dependent photocatalytic H_2 evolution and b) Hydrogen-evolution rate over different samples under visible-light illumination ($\lambda > 420\,nm$). c) UV–vis DRS for different samples.
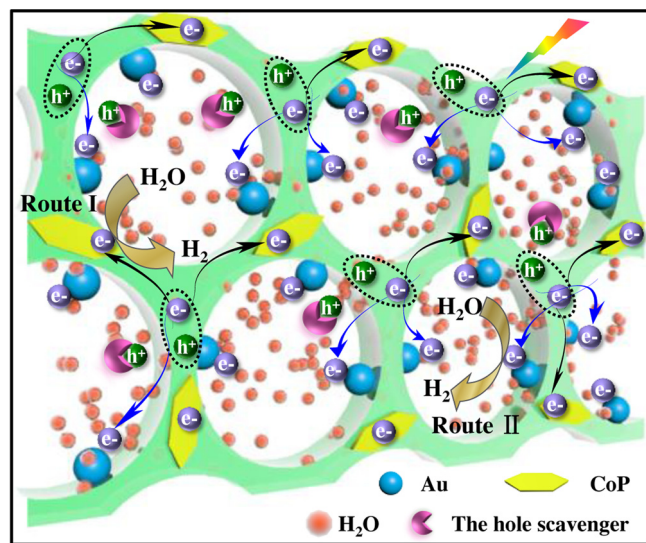

Fig. 11. Schematic illustration of charge transfer in the spatially separated CoP/3DOM g-C_3N_4/Au for photocatalytic H_2 evolution.

show that the spatial positioning effect of dual cocatalysts (inside Au and outside CoP) can greatly enhance the visible-light absorption capacity, thus promoting the generation of charges in the H_2 evolution reaction to enhance the photocatalytic activity of ACC samples.

Secondly, and more importantly, the spatial positioning effect of dual cocatalysts can significantly enhance the charge transfer capacity of ACC samples, and its cocatalytic mechanism can be well revealed by the schematic illustration in Fig. 11. Under the visible-light irradiation ($\lambda > 420\,nm$), the charge carriers (electron-hole pairs) are motivated from the walls of 3DOM g-C_3N_4. Then the photogenerated holes are

immediately consumed by the massive hole scavengers, while the photoexcited electrons can fast transfer to the surface of Au or CoP owing to the above-mentioned spatial positioning effect of dual cocatalysts. With this process, the recombination of electron-hole pairs is effectively suppressed. In the CoP/3DOM g-C_3N_4/Au sample, the dual cocatalysts with spatially separated positioning can provide two opposite unidirectional electron migration routes to significantly accelerate the process of electron transfer. Route I is that the electrons transfer along the g-C_3N_4 walls to CoP nanosheets on the outside surface of 3DOM framework, due to the presence of built-in electric field orienting from 3DOM g-C_3N_4 towards CoP nanosheets, which can be easily formed owing to the lower reduction potential of CoP than that of g-C_3N_4 [49,50], and the CoP cocatalyst can offer plentiful catalytic active sites for the adsorption of H^+ and enable the electrons to interact with these adsorbed H^+ to generate H_2 [15,22]. Similarly, route II is that the electrons transfer towards the inside surface of 3DOM framework to reach Au nanoparticles, this is because that the Fermi level of Au nanoparticles is lower than the reduction potential of 3DOM g-C_3N_4, thus producing a built-in electric field from g-C_3N_4 towards Au [51–53]. Ultimately, these electrons reduce H^+ to H_2 on the surface of Au nanoparticles [53–55]. As a result, the above two routes endowed by dual cocatalysts with spatially separated positioning can greatly promote charge tansfer in two opposite directions, thus achieving high-efficiency charge transfer for ACC samples, eventually resulting in a remarkable photocatalytic hydrogen evolution.

Additionally, the average wall thickness of 3DOM g-C_3N_4 framework is another important factor to influence the photocatalytic activity of ACC series samples. According to the SEM, TEM and ICP-MS results, it is easily found that ACC4 and ACC5 have the same spatial positioning of dual cocatalysts as well as the very close content of Au and CoP, meanwhile, ACC4 and ACC5 show the similar optical absorption ability (UV–vis DRS in Fig. 9a), active surface area and pore volume (Table S2), but the only difference between the two samples is that ACC4 (avg.

80 nm) has a smaller average wall thickness than ACC5 (avg. 120 nm). With this structural characteristic, ACC4 exhibits an outstanding activity of H_2 generation (11,820.1 $\mu mol\,h^{-1}\,g^{-1}$), far outperforming ACC5 (4938.5 $\mu mol\,h^{-1}\,g^{-1}$), it is due to the fact that the proper average wall thickness with an optimal charge transfer distance can efficiently enhance the charge separation (Fig. 9c-f). This point can be further evidenced by the comparison of ACC3 (avg. 40 nm) and ACC4 (avg. 80 nm). In addition to their average wall thickness, it can be seen that the two sampes have the same spatial positioning and loading content of dual cocatalysts, meanwhile, ACC3 also shows much stronger optical absorption ability (Fig. 9a) and slightly higher active surface area as well as pore volume (Table S2) than ACC4. However, ACC3 (7960.7 $\mu mol\,h^{-1}\,g^{-1}$) dispalys much lower HER activity than that of ACC4 (11,820.1 $\mu mol\,h^{-1}\,g^{-1}$), suggesting that the much smaller average wall thickness is not conducive to improve the charge transfer efficiency (Fig. 9c–f). Therefore, it can be well concluded that when the average wall thickness was precisely controlled to be 80 nm, the ACC4 sample has the optimal charge transfer distance from the walls of 3DOM g-C_3N_4 framework to the surface of Au or CoP, which means that massive photogenerated charges can efficiently transfer to the surface of cocatalysts and participate in photocatalytic reaction, thereby resulting in the enhancement of photocatalytic hydrogen evolution activity.

Based on all the above discussion related to the origin of remarkable photocatalytic activity of CoP/3DOM g-C_3N_4/Au, we can draw a conclusion that the synergistic function of spatial positioning effect of dual cocatalysts and optimal charge transfer distance could significantly promote the charge generation and trasfer of CoP/3DOM g-C_3N_4/Au (ACC4), eventually contributing to the outstanding photocatalytic hydrogen evolution (11,820.1 $\mu mol\,h^{-1}\,g^{-1}$) and high AQE values (37.1% at 365 nm, 27.6% at 435 nm and 29.9% at 550 nm).

5. Conclusion

In summary, we have constructed the spatially separated CoP/3DOM g-C_3N_4/Au ternary composite photocatalyst. In the CoP/3DOM g-C_3N_4/Au composite, the Au nanoparticles and CoP nanosheets are separately anchored on the inside and outside surface of 3DOM g-C_3N_4 framework to realize the construction of dual cocatalysts with spatially separated positioning. Moreover, the average wall thickness of 3DOM g-C_3N_4 was precisely controlled with the different SiO_2 diameters to manipulate the charge transfer distance (from 3DOM g-C_3N_4 walls to the surface of cocatalysts). The results show that the dual cocatalysts with spatially separated positioning and optimal charge transfer distance together result in the greatly enhanced charge transfer capacity of ACC4 sample, eventually contributing to a remarkable photocatalytic H_2 evolution activity. This work would provide a new platform to design high-performance artificial photocatalysts with outstanding charge transfer capacity.

Acknowledgements

Appendix A. Supplementary data

Supplementary material related to this article can be found, in the online version, at doi:https://doi.org/10.1016/j.apcatb.2018.10.029.

References

[1] M. Liu, Y. Chen, J. Su, J. Shi, X. Wang, L. Guo, Nat. Energy 1 (2016) 16151.
[2] L. Li, J. Yan, T. Wang, Z. Zhao, J. Zhang, J. Gong, N. Guan, Nat. Commun. 6 (2015) 5881.
[3] V.W.H. Lau, V.W.Z. Yu, F. Ehrat, T. Botari, I. Moudrakovski, T. Simon, V. Duppel, E. Medina, J.K. Stolarczyk, J. Feldmann, V. Blum, B.V. Lotsch, Adv. Energy Mater. 7 (2017) 1602251.
[4] W. Bi, X. Li, L. Zhang, T. Jin, L. Zhang, Q. Zhang, Y. Luo, C. Wu, Y. Xie, Nat. Commun. 6 (2015) 8647.
[5] B. Lin, H. Li, H. An, W. Hao, J. Wei, Y. Dai, C. Ma, G. Yang, Appl. Catal. B: Environ. 220 (2018) 542–552.
[6] W. Chen, Y. Hua, Y. Wang, T. Huang, T. Liu, X. Liu, J. Catal. 349 (2017) 8–18.
[7] A. Li, T. Wang, X. Chang, W. Cai, P. Zhang, J. Zhang, J. Gong, Chem. Sci. 7 (2016) 890–895.
[8] S. Song, J. Wang, T. Peng, W. Fu, L. Zan, Appl. Catal. B: Environ. 228 (2018) 39–46.
[9] J. Ran, G. Gao, F. Li, T. Ma, A. Du, S. Qiao, Nat. Commun. 8 (2017) 13907.
[10] H. Yu, X. Huang, P. Wang, J. Yu, J. Phys. Chem. C 120 (2016) 3722–3730.
[11] Q. Li, C. Cui, H. Meng, J. Yu, Chem. Asian J. 9 (2014) 1766–1770.
[12] J. Zhao, X. Yan, N. Zhao, X. Li, B. Lu, X. Zhang, H. Yu, RSC Adv. 8 (2018) 4979–4986.
[13] D. Wang, T. Hisatomi, T. Takata, C. Pan, M. Katayama, J. Kubota, K. Domen, Angew. Chem. Int. Ed. 52 (2013) 11252–11256.
[14] D. Zheng, X. Cao, X. Wang, Angew. Chem. Int. Ed. 55 (2016) 11512–11516.
[15] M. Xing, B. Qiu, M. Du, Q. Zhu, L. Wang, J. Zhang, Adv. Funct. Mater. 27 (2017) 1702624.
[16] B. Lin, G. Yang, B. Yang, Y. Zhao, Appl. Catal. B: Environ. 198 (2016) 276–285.
[17] K. Ji, H. Arandiyan, P. Liu, L. Zhang, J. Han, Y. Xue, J. Hou, H. Dai, Nano Energy 27 (2016) 515–525.
[18] K. Ji, J. Deng, H. Zang, J. Han, H. Arandiyan, H. Dai, Appl. Catal. B: Environ. 165 (2015) 285–295.
[19] Y. Chang, K. Yu, C. Zhang, Z. Yang, Y. Feng, H. Hao, Y. Jiang, L. Lou, W. Zhou, S. Liu, Appl. Catal. B: Environ. 215 (2017) 74–84.
[20] X. Yan, M. Xia, B. Xu, J. Wei, B. Yang, G. Yang, Appl. Catal. B: Environ. 232 (2018) 481–491.
[21] X. Wang, S. Feng, W. Zhao, D. Zhao, S. Chen, New J. Chem. 41 (2017) 9354–9360.
[22] C. Li, Y. Du, D. Wang, S. Yin, W. Tu, Z. Chen, M. Kraft, G. Chen, R. Xu, Adv. Funct. Mater. 27 (2017) 1604328.
[23] S.S. Yi, J.M. Yan, B.R. Wulan, S.J. Li, K.H. Liu, Q. Jiang, Appl. Catal. B: Environ. 200 (2017) 477–483.
[24] J. Zhang, M. Zhang, G. Zhang, X. Wang, ACS Catal. 2 (2012) 940–948.
[25] D. Zheng, G. Zhang, X. Wang, Appl. Catal. B: Environ. 179 (2015) 479–488.
[26] K. Chen, X. Zhang, X. Yang, M. Jiao, Z. Zhou, M. Zhang, D. Wang, X. Bu, Appl. Catal. B: Environ. 238 (2018) 263–273.
[27] X. Wei, C. Shao, X. Li, N. Lu, K. Wang, Z. Zhang, Y. Liu, Nanoscale 8 (2016) 11034–11043.
[28] K. Yang, C. Meng, L. Lin, X. Peng, X. Chen, X. Wang, W. Dai, X. Fu, Catal. Sci. Technol. 6 (2016) 829–839.
[29] D. Dai, H. Xu, L. Ge, C. Han, Y. Gao, S. Li, Y. Lu, Appl. Catal. B: Environ. 217 (2017) 429–436.
[30] Z. Pan, Y. Zheng, F. Guo, P. Niu, X. Wang, ChemSusChem 10 (2017) 87–90.
[31] M.K. Bhunia, S. Melissen, M.R. Parida, P. Sarawade, J.M. Basset, D.H. Anjum, O.F. Mohammed, P. Sautet, T.L. Bahers, K. Takanabe, Chem. Mater. 27 (2015) 8237–8247.
[32] N. Tian, Y. Zhang, X. Li, K. Xiao, X. Du, F. Dong, G.I.N. Waterhouse, T. Zhang, H. Huang, Nano Energy 38 (2017) 72–81.
[33] R.A. Rather, S. Singh, B. Pal, Appl. Catal. B: Environ. 213 (2017) 9–17.
[34] A. Tanaka, K. Hashimoto, H. Kominami, J. Am. Chem. Soc. 136 (2014) 586–589.
[35] A. Tanaka, K. Hashimoto, H. Kominami, Chem. Commun. 53 (2017) 4759–4762.
[36] Y. Shi, J. Wang, C. Wang, T.T. Zhai, W.J. Bao, J.J. Xu, X.H. Xia, H.Y. Chen, J. Am. Chem. Soc. 137 (2015) 7365–7370.
[37] Q. Peng, H. Zhao, L. Qian, Y. Wang, G. Zhao, Appl. Catal. B: Environ. 174-175 (2015) 157–166.
[38] J. Jiao, Y. Wei, Z. Zhao, J. Liu, J. Li, A. Duan, G. Jiang, Ind. Eng. Chem. Res. 53 (2014) 17345–17354.
[39] J. Di, J. Xia, X. Li, M. Ji, H. Xu, Z. Chen, H. Li, Carbon 107 (2016) 1–10.
[40] J. Xu, F. Wu, Q. Jiang, Y.X. Li, Catal. Sci. Technol. 5 (2015) 447–454.
[41] N. Perret, R. Wang, L. Delannoy, C. Potvin, C. Louis, M.A. Keane, J. Catal. 286 (2012) 172–183.
[42] P. Selvakannan, K. Mantri, J. Tardio, S.K. Bhargava, J. Colloid, Interf. Sci. 394 (2013) 475–484.
[43] X. Zhang, T. Peng, L. Yu, R. Li, Q. Li, Z. Li, ACS Catal. 5 (2014) 504–510.
[44] M. Ji, J. Di, Y. Ge, J. Xia, H. Li, Appl. Surf. Sci. 413 (2017) 372–380.
[45] J. Xia, M. Ji, J. Di, B. Wang, S. Yin, Q. Zhang, M. He, H. Li, Appl. Catal. B: Environ. 191 (2016) 235–245.
[46] P. Niu, L. Zhang, G. Liu, H.M. Cheng, Adv. Funct. Mater. 22 (2012) 4763–4770.
[47] X. Zhang, L. Yu, C. Zhuang, T. Peng, R. Li, X. Li, ACS Catal. 4 (2014) 162–170.
[48] J. Di, J. Xia, H. Li, Z. Liu, Nano Energy 35 (2017) 79–91.
[49] X.J. Wang, X. Tian, Y.J. Sun, J.Y. Zhu, F.T. Li, H.Y. Mu, J. Zhao, Nanoscale 10 (2018) 12315–12321.
[50] H. Zhao, P. Jiang, W. Cai, Chem. Asian J. 12 (2017) 361–365.
[51] Y. Fu, T. Huang, B. Jia, J. Zhu, X. Wang, Appl. Catal. B: Environ. 202 (2017) 430–437.

[52] X. Zhou, G. Zhang, C. Shao, X. Li, X. Jiang, Y. Liu, Ceram. Int. 43 (2017) 15699–15707.

[53] S. Samanta, S. Martha, K. Parida, ChemCatChem 6 (2014) 1453–1462.

[54] X. Yu, A. Shavel, X. An, Z. Luo, M. Ibanez, A. Cabot, J. Am. Chem. Soc. 136 (2014) 9236–9239.

[55] G.L. Chiarello, E. Selli, L. Forni, Appl. Catal. B: Environ. 84 (2008) 332–339.